Spatio-Temporal Distribution Characteristics of Global Annual Maximum Land Surface Temperature Derived from MODIS Thermal Infrared Data From 2003 to 2019

Si-Bo Duan, *Senior Member, IEEE*, Cheng Huang, Xiangyang Liu, Meng Liu, Yingwei Sun, and Caixia Gao

***Abstract*—Land surface temperature (LST) is an important parameter in the physical processes of energy and water balance at the local and global scales. The annual maximum composite of LST provides important information about ecosystem exposure patterns to extreme LST. It has the ability to characterize the changes associated with extreme climatic events and significant land-cover changes. In this study, the spatio-temporal distribution characteristics of global annual maximum LST extracted from the MODIS LST product (MYD11A1) during the period 2003–2019 were investigated. The results indicate that the spatial pattern of annual maximum LST is associated with the biophysical and biogeographic factors of Earth's ecosystems. The interannual variability of annual maximum LST during the period 2003–2019 is relatively small. The changing trend of annual maximum LST during the period 2003–2019 in the globe is 0.1°C/decade. The annual maximum LST data was applied to detect thermal anomalies, including drought, heat waves, and ice melting. Some significant thermal anomaly events were well identified using the annual maximum LST data with a standardized anomaly index larger than 2.5.**

***Index Terms*—Annual maximum land surface temperature (LST), MODIS, spatio-temporal variability, thermal anomaly detecting.**

I. Introduction

LAND surface temperature (LST) is an important parameter in the physical processes of energy and water balance at the interface between the land surface and the atmosphere [1], [2]. It has been applied in a variety of studies, e.g., drought monitoring [3], [4], thermal environment monitoring [5]–[7], and global climate change [8]–[11]. LST is identified as a key Earth Science Data Record by the National Aeronautics and Space Administration and as one of the ten Essential Climate Variables in the land biosphere by the Global Climate Observing System [12].

Satellite thermal infrared (TIR) remote sensing provides the best way to measure LST with high spatial resolution at regional and global scales [13], [14]. Accurate knowledge of the spatio-temporal variability of LST is crucial for detecting changes in land surface characteristics and understanding climate change. In current years, the analysis of the spatio-temporal distribution characteristics of satellite-derived LST has gained more and more attention. For example, Sismanidis *et al.* [15] explored the spatio-temporal dynamics of LST during the period 2009–2013 over Europe. Zhao *et al.* [16] analyzed the spatio-temporal variability of LST from 2000 to 2017 over the mountainous area affected by the 2008 Wenchuan earthquake by using an annual temperature cycle model and the Mann-Kendall test. Prakash and Norouzi [17] examined the interannual variability of LST across India for the period from 2003 to 2017 in terms of a linear trend analysis. Yu *et al.* [18] investigated the interannual spatio-temporal variability of LST in China from 2003 to 2018 by using a continuous and derivable annual temperature cycle model. These studies are helpful for characterizing the thermal behavior of the Earth's surface and understanding climate change.

Due to the inability of penetrating clouds, TIR-based LST is limited to clear-sky conditions, which leads to spatial incompleteness of LST [19]. By removing the natural synoptic variability of daily LST and focusing on the highest LST at an annual scale, the annual maximum composite of LST can provide a spatially continuous LST map [20]. Annual maximum LST is a unique and informative annual monitoring metric for integrating the biophysical influence of land cover and the consequences of changes across the Earth's land surface [21]. It can characterize the changes associated with extreme climatic events (e.g., heat waves and droughts) and significant land cover changes [22].

The main objective of this study is to analyze the spatio-temporal distribution characteristics of global annual maximum LST derived from MODIS TIR data from 2003 to 2019. This article is organized as follows. Section II introduces the data

Manuscript received January 11, 2022; revised April 7, 2022; accepted June 1, 2022. Date of publication June 7, 2022; date of current version June 17, 2022. This work was supported in part by the National Key R&D Program of China, under Grant 2018YFB0504800 and Grant 2018YFB0504804 and in part by the National Natural Science Foundation of China under Grant 41871275 and Grant 42101373. *(Corresponding author: Cheng Huang.)*

Si-Bo Duan, Cheng Huang, Xiangyang Liu, Meng Liu, and Yingwei Sun are with the Key Laboratory of Agricultural Remote Sensing, Ministry of Agriculture/Institute of Agricultural Resources and Regional Planning, Chinese Academy of Agricultural Sciences, Beijing 100081, China (e-mail: duansibo@caas.cn; huangcheng9960@126.com; liuxiangyang@caas.cn; liumeng@caas.cn; sunyingwei@caas.cn).

Caixia Gao is with the Key Laboratory of Quantitative Remote Sensing Information Technology, Aerospace Information Research Institute, Chinese Academy of Sciences, Beijing 100094, China (e-mail: gaocaixia@aoe.ac.cn).

Digital Object Identifier 10.1109/JSTARS.2022.3181051

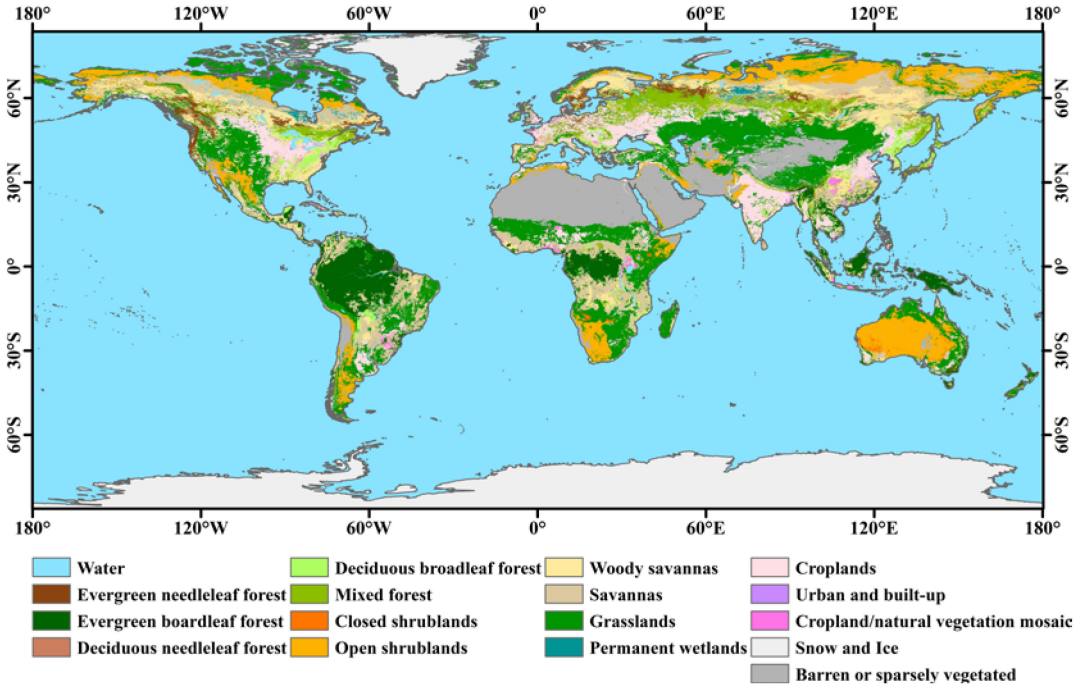

Fig. 1. Map of global land cover types in 2019.

and methods used in this study. Section III presents the results of spatio-temporal variability of global annual maximum LST and its application in thermal anomaly detection. The conclusion is given in Section IV.

II. Data and Methods

A. MODIS Data

The Moderate Resolution Imaging Spectroradiometer (MODIS) is one of the key instruments onboard the Terra and Aqua satellites. The Terra overpass time is around 10:30 a.m. local solar time in descending mode, while the Aqua overpass time is around 1:30 p.m. local solar time in ascending mode. MODIS has 36 spectral bands from visible and near infrared to thermal infrared, which provides global coverage every 1 to 2 days during daytime and nighttime.

The MODIS LST product MxD11A1 at 1-km spatial resolution was generated from TIR data in MODIS bands 31 and 32 using the generalized split-window algorithm [23]. Taking into account that the Aqua overpass time is more close to the time of daily maximum and minimum temperature, the MYD11A1 Version 6 product during the period 2003–2019 was used to extract annual maximum LST. The MODIS Reprojection Tool (MRT) was used to process the MYD11A1 product from a sinusoidal projection to a geographical projection. In this study, the pixels with QC flags of "clear-sky," "average LST error $\leq$ 1 K/2 K," and "average emissivity error $\leq$ 0.01/0.02" were identified as valid pixels. In addition, the aqua thermal anomalies and fire daily (MYD14A1) Version 6 product was used to remove fire pixels. MYD14A1 data were mosaicked and reprojected using MRT in a similar procedure to MYD11A1 LST data to match its projection type, pixel size, and time interval. Therefore, MYD11A1 LST pixels can be filtered if they are corresponding to pixels with flags "Fire (low confidence)," "Fire (normal confidence)" and "Fire (high confidence)."Fig. 1 shows the map of global land cover types in 2019 obtained from MCD12C1 Version 6 land cover type products.

B. Trend Analysis

A linear regression method is used to analyze the change trend in annual maximum LST ($\mathrm{LST_{am}}$) during the period 2003–2019, which reflects the interannual variability in $\mathrm{LST_{am}}$. The formula is expressed as follows [24]:

$$\theta_{\mathrm{slope}} = \frac{n \times \sum_{i=1}^{n} i \times LST_{am,i} - \sum_{i=1}^{n} i \sum_{i=1}^{n} LST_{am,i}}{n \times \sum_{i=1}^{n} i^2 - \left(\sum_{i=1}^{n} i\right)^2} \tag{1}$$

where θ_{slope} is the change rate of $\mathrm{LST_{am}}$ during the period 2003–2019, n is the number of years ($n = 17$), i is the ith year, and $\mathrm{LST_{am,i}}$ is the value of $\mathrm{LST_{am}}$ in the ith year. $\theta_{\mathrm{slope}} > 0$ shows an increasing trend in $\mathrm{LST_{am}}$, whereas $\theta_{\mathrm{slope}} < 0$ indicates a decreasing trend.

C. Thermal Anomalies Detecting

The standardized anomalies of $\mathrm{LST_{am}}$ are calculated by dividing $\mathrm{LST_{am}}$ anomalies by the standard deviation of $\mathrm{LST_{am}}$ during the period 2003–2019. They generally provide more information about the magnitude of the anomalies because influences of dispersion have been removed [27]. The formula is written as follows:

$$SAI = \frac{LST_{am} - \mu}{\sigma} \tag{2}$$

where SAI is the standardized anomaly index of LST_{am}, of which the value indicates the normalized level of anomaly. The higher SAI is, the abnormal the LST_{am} is relative to other years. Operationally, a value of SAI higher than 2.5 is considered as typical anomaly in samples. μ is the mean of LST_{am} time series for the period 2003–2019, and σ is the standard deviation of LST_{am} time series for the period 2003–2019.

D. Spatial Analysis

Spatial analysis is the quantitative study of geospatial phenomena to extract the spatial information implied in data. LST is a variable that is closely relating to other geographical, climatological, and hydrological elements.

Compared with daily instantaneous LST that is associated with synoptic weather variability, annual maximum value composites remove natural synoptic variability and provide spatially continuous LST at the global scale. A global map of LST_{am} provides a unique way to characterize the LST gradient associated with land cover types, e.g., the transition from low LST_{am} in ice/snow areas, to medium LST_{am} in vegetated areas, and high LST_{am} in barren areas. Therefore, the uniqueness of LST_{am} has the potential to indicate large-scale land cover change or monitor thermal anomalies, e.g., heat waves and droughts.

III. Results and Discussion

A. Spatial Pattern of Annual Maximum LST

Fig. 2 shows the spatial distribution of multiyear mean and trend of LST_{am} during the period 2003–2019. From Fig. 2a, we can see that there is a high correlation between the spatial pattern of LST_{am} and land cover types. Higher mean LST_{am} of larger than 60°C occurs between 30° S and 30° N latitude, where the land cover types are dominated by desert surfaces, e.g., the Sahara Desert in North Africa, the Arabian Desert in Arabian Peninsula, the North American Desert, the Deserts of Australia, and the Taklamakan Desert in China. The lowest mean LST_{am} is located in the South Pole. Greenland in the North Pole also has relatively low mean LST_{am}. As shown in Fig. 2b, significant warming trends occur in central Russia and eastern Kazakhstan, whereas significant cooling trends are found in the central United States, northwestern Kazakhstan, and central and northern China. The spatial variability of LST_{am} was compared with the mean LST variability of Sobrino's research, in which the trend and distribution of mean LST are analyzed [28], [29]. The spatial distribution of the multiyear trend of LST_{am} is under that of Sobrino and Julian's maximum LST during 2000–2011 [29]. In spite that LST_{am} and mean LST represent different features of the land surface, the spatial distribution of LST_{am} and mean LST shows a similar pattern, featuring a distinct increase in middle Europe and Siberia and a decrease in northern America and northeast Asia.

To further describe the characteristics of LST_{am}, Fig. 3 displays the density probability of LST_{am} for every 1-km^2 pixel across the global land surface during the period 2003–2019. Although small variations exist in the density probability for each year, a similar multimodal distribution that is associated with the biophysical and biogeographic factors of Earth's ecosystems across 17 years of LST_{am} can be observed in Fig. 3. Ice/snow areas account for the low-temperature mode with LST_{am} of approximately −30°C to 0°C, whereas shrubland and barren areas are reflected in the high-temperature mode with LST_{am} of approximately 50°C to 65°C. Forest, woody savannas, and wetland areas are located in the range from approximately 20°C to 35°C, and savannas, grassland, cropland, and urban areas fall in the range from approximately 30°C to 50°C.

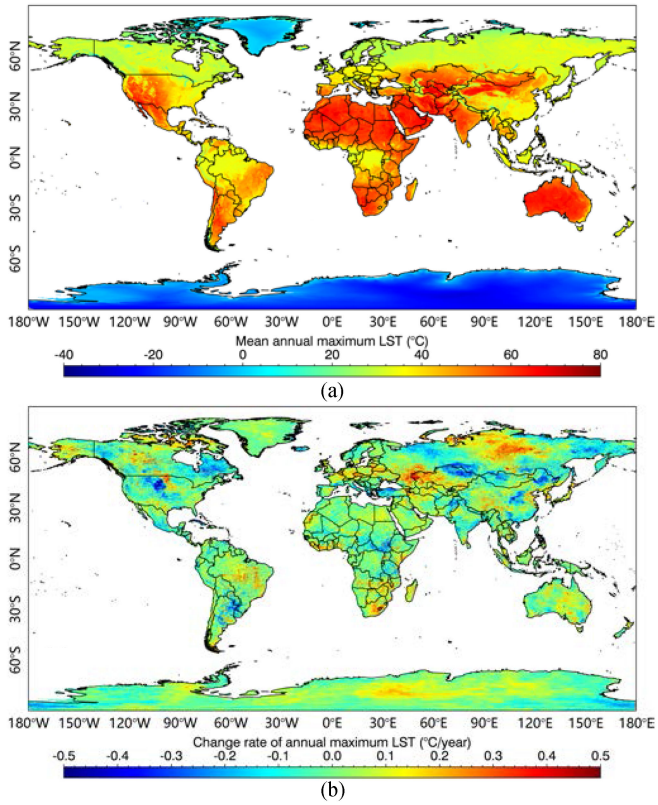

Fig. 2. Spatial distribution of multiyear. (a) Mean and (b) Trend of LST_{am} during the period 2003–2019.

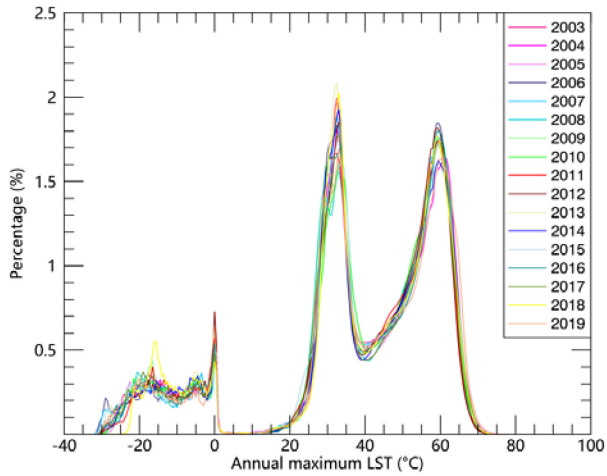

Fig. 3. Density probability of LST_{am} for every 1-km^2 pixel across the global land surface during the period 2003–2019.

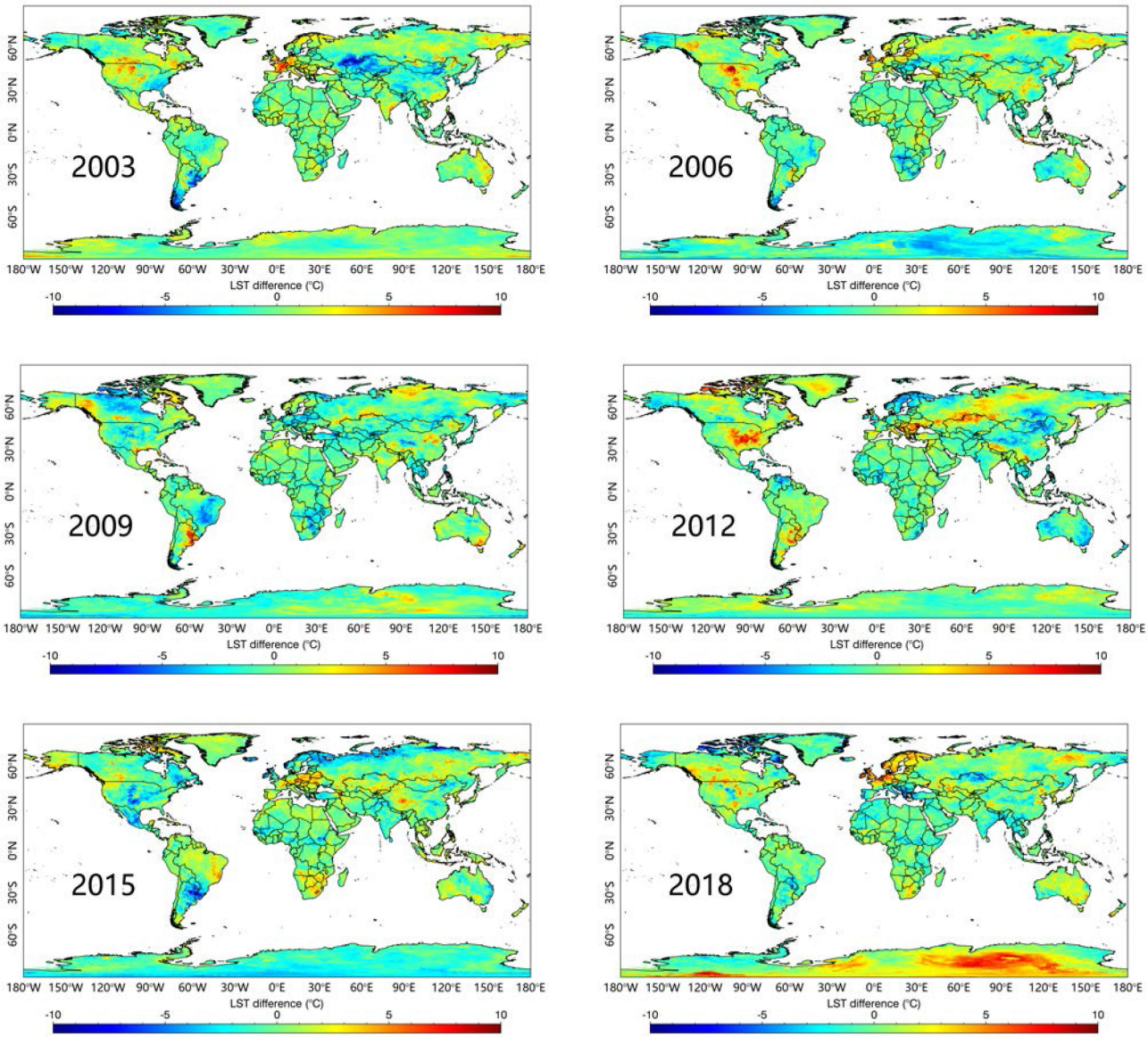

Fig. 4. Spatial distribution of discrepancy of LST_{am} in 2003, 2006, 2009, 2012, 2015, and 2018.

Fig. 4 shows the spatial distribution of discrepancy from the average of LST_{am} during the period 2003–2019 with an increment of three years. As shown in Fig. 4, there is small interannual variability in the spatial pattern of discrepancy of LST_{am} for most of the areas around the globe. However, intense LST_{am} anomalies in specific areas can still be interpreted from Fig. 4, e.g., the large patch of red areas in North America in 2012. The color map in 2018 shows an overall warmer hue than that in 2003, by LST_{am} trend during this period.

B. Temporal Variability of Annual Maximum LST

Fig. 5 shows the interannual variability of mean LST_{am} during the period 2003–2019 over different regions, including the Globe (GB), the Northern Hemisphere (NH), the Southern Hemisphere (SH), NH high latitudes (60°–90° N), NH middle latitudes (30°–60° N), NH low latitudes (0°–30° N), SH low latitudes (0°–30° S), SH middle latitudes (30°–60° S), and SH high latitudes (60°–90° S). It is worth noting that the mean and trend values in Fig. 5 and Table I were calculated in an area-weighted way (instead of simply adding up pixels in Fig. 2) for more accurate statistics. The multiyear mean and trend of LST_{am} during the period 2003–2019 over different regions are summarized in Table I.

The mean temperature in SH low latitude region and SH middle latitude region is approximate, while the temperature in NH low latitude region and NH middle latitude region shows distinguishable discrepancy. The main factors of these phenomena are the influence of land cover and climate type of these regions. Africa savannah and Amazon rainforest take a high proportion of SH low latitude region. These two areas feature high vegetation coverage and low temperature comparing with bare soil surfaces at SH middle latitude region, e.g., the Australia desert. At Northern Hemisphere, the existence of the Sahara

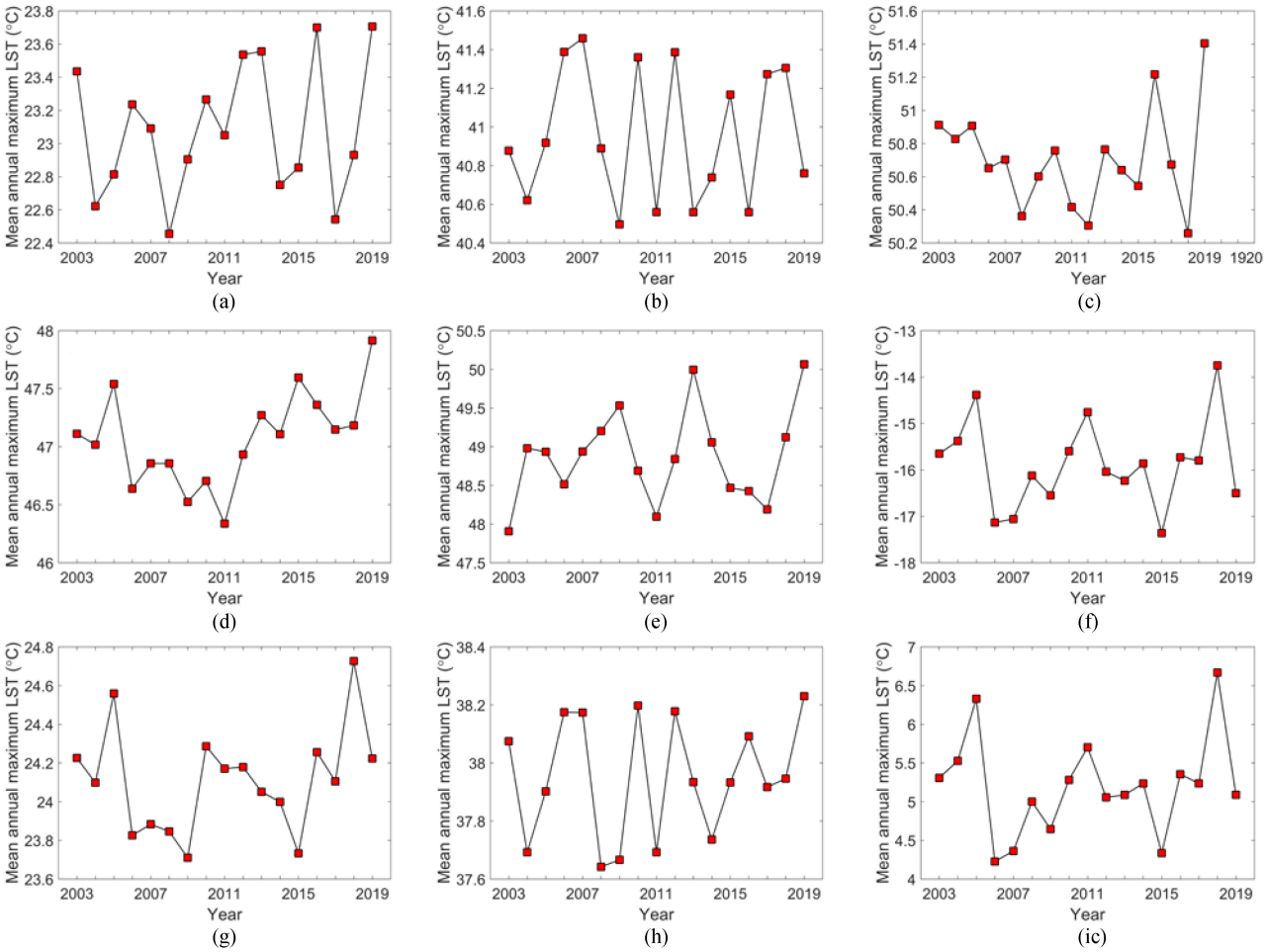

Fig. 5. Interannual variability of mean LST_{am} over different regions during the period 2003–2019, including (a) NH high latitudes (60°–90° N), (b) NH middle latitudes (30°–60° N), (c) NH low latitudes (0°–30° N), (d) SH low latitudes (0°–30° S), (e) SH middle latitudes (30°–60° S), (f) SH high latitudes (60°–90° S), (g) the NH, (h) the SH, and (i) the GB.

TABLE I
MULTIYEAR MEAN AND TREND OF LST_{AM} DURING THE PERIOD 2003–2019 OVER DIFFERENT REGIONS

Region	Mean (°C)	Trend (°C/decade)
60°-90° N	23.08	0.160
30°-60° N	40.96	0.009
0°-30° N	50.70	0.036
0°-30° S	47.06	0.350
30°-60° S	48.88	0.297
60°-90° S	-15.88	0.071
NH	37.95	0.062
SH	5.20	0.161
GB	24.11	0.104

Desert raises the mean maximum temperature in NH low latitude region, meanwhile monsoon climates combined with high vegetation in NH middle latitude region lower the temperature, causing distinguishable difference between these two areas.

The mean LST_{am} in the Globe is 24.1°C. Comparing with that of 38.0°C in the NH, the mean LST_{am} of 5.2°C in the SH is lower. The lowest mean LST_{am} of −15.9°C occurs in the SH high latitude region with most permanent snow and ice surfaces, whereas the highest mean LST_{am} of 50.7°C appears in the NH low latitude region with most desert surfaces.

As shown in Table I, warming trends of LST_{am} are observed over all regions. The trend of LST_{am} in the Globe is 0.1°C/decade, and the trend of LST_{am} in the SH at a rate of 0.16°C/decade is approximately 2.5 times greater than that in the NH at a rate of 0.06°C/decade. The highest trend at a rate of 0.35°C/decade occurs in the SH low latitude region, whereas the lowest trend at a rate of 0.009°C/decade appears in the NH middle latitude region. Relatively higher trend is also found in the SH middle latitude region.

The temporal variation of LST_{am} was also compared with LST trend of Sobrino's research in 2020 [28]. Both mean LST and LST_{am} show a distinguishable uprising trend during 2003–2019. The piecewise trends also show some synchronous patterns in mean LST and LST_{am}, e.g., high mean LST and LST_{am} occur at 2005 and 2016.

Compared with mean LST during 2003–2019, LST_{am} presents a similar uprising trend at latitudinal, hemispherical, and global scales. Especially, in correspondence with mean LST,

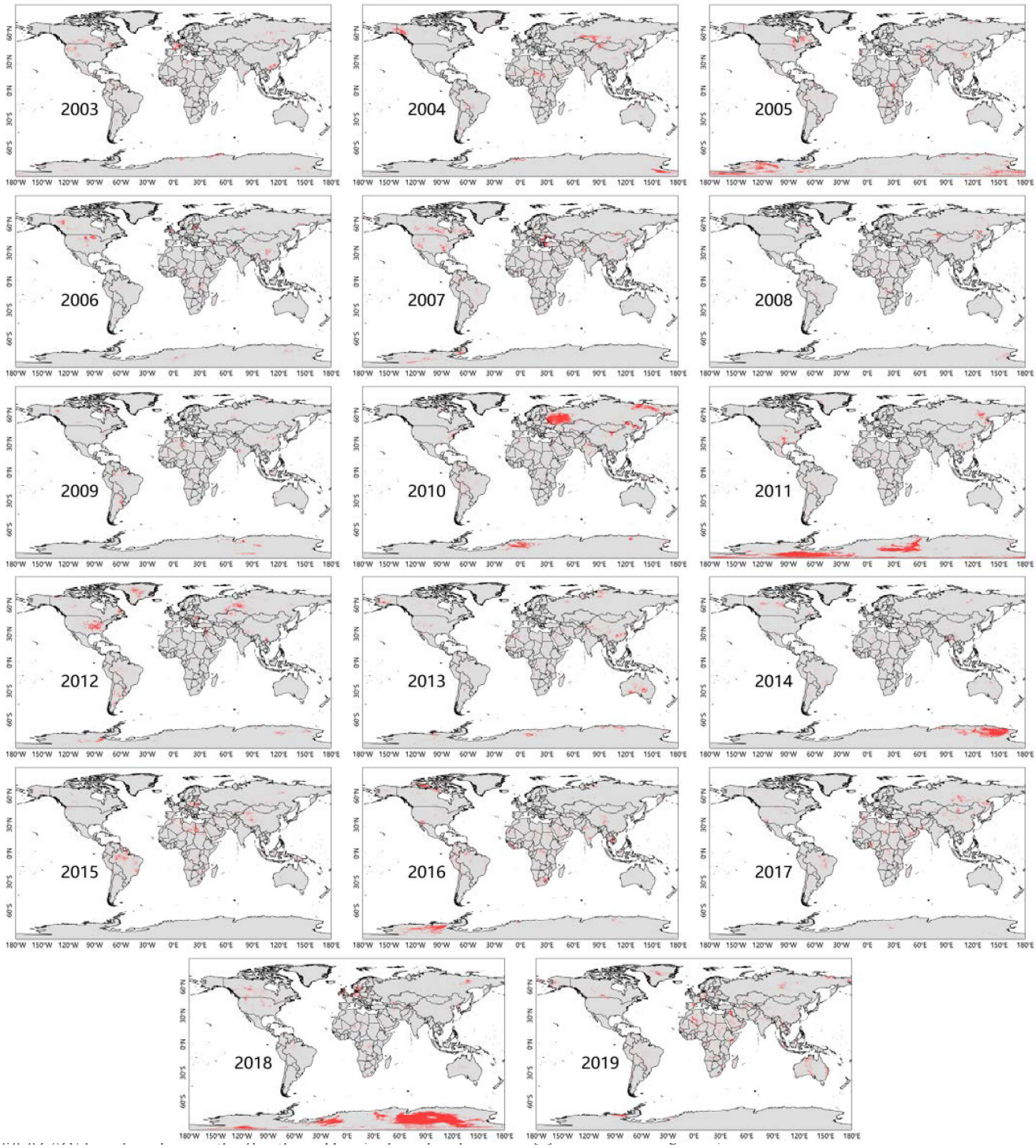

Fig. 6. Spatial distribution of SAI $>$ 2.5 during the period 2003–2019.

$\mathrm{LST_{am}}$ at NH high latitudes, SH low latitudes, and SH middle latitudes show a more distinct uprising trend compared with other latitudinal regions.

C. Application of Annual Maximum LST

The annual maximum LST data were used to detect thermal anomalies during the period 2003–2019. To depict the results more clearly, Fig. 6 only shows the spatial distribution of SAI $>$ 2.5, which is regarded as intense thermal anomalies taking previous studies as reference [21]. The threshold of SAI$>$2.5 is an optimized value that balances indicating intense thermal anomaly and filtering irrelevant thermal fluctuation. The significant change of $\mathrm{LST_{am}}$ has the potential to indicate large-scale land cover change or monitor thermal anomalies, e.g., drought, heat wave, and ice melting.

A drought is a prolonged shortage of available water, primarily due to insufficient precipitation. Two severe droughts in the United States in 2012 and in Amazon rain forest in 2015 are observed in Fig. 6. In 2012, more than two-thirds of counties in the United States were declared to be drought disaster areas. This was the most severe and extensive drought in the United States in over 50 years [30]. In 2015, a record-breaking extreme drought occurred in the Amazon rain forest, which was associated with the El Niño/Southern Oscillation [31].

A heat wave is an unusually hot weather phenomenon, which has enormous adverse social, economic, and environmental impacts. Two severe heat waves are seen in Fig. 6, i.e., the 2003 European heat wave and the 2010 Russian heat wave. The 2003 European heat wave is the hottest summer on record in Europe since 1540 [32]. The 2010 Russian heat wave was a record-breaking event by nearly any description [33].

The Greenland ice sheet is a major contributor to global sea-level rise in recent decades [34]. Two massive ice melts in Greenland in 2012 and 2019 can be observed in Fig. 6. The summer of 2012 brought record-breaking melt to Greenland since 1979 [35], [36]. It was the first year in the satellite record that nearly the entire ice sheet experienced surface melting. When considering the overall melt extent, 2019 is comparable to 2012, with approximately 95% of the entire ice sheet undergoing surface melting.

These anomaly events abovementioned are just taken as examples to show the ability of annual maximum LST data for detecting thermal anomalies. The spatial distribution of thermal anomalies reflects extreme anomaly events to a certain extent. It should be noted that not all anomaly patches are indicative of thermal anomaly events. For instance, there is a large red patch can be observed in Antarctica in 2011 and 2018. However, there is no reported thermal anomaly in Antarctica during the period of this research. Therefore, the red patch might be caused by LST accuracy problem in ice covered areas.

IV. Conclusion

In this study, the spatio-temporal distribution characteristics of global annual maximum LST extracted from the MYD11A1 LST product during the period 2003–2019 were analyzed. Because LST is mainly driven by incoming solar radiation, the interannual variability in the spatial pattern of annual maximum LST is small. The spatial distribution of annual maximum LST at the global scale is associated with the biophysical and biogeographic factors of Earth's ecosystems. Therefore, annual maximum LST provides a unique way to obtain spatially continuous LST map for characterizing changes associated with extreme climatic events and significant land-cover changes.

There is small interannual variability of mean annual maximum LST during the period 2003–2019. The mean of annual maximum LST in the Globe is 24.1°C with a change trend of 0.1°C/decade. The NH has higher annual maximum LST of 38.0°C with a smaller change trend of 0.06°C/decade, whereas the SH has lower annual maximum LST of 5.2°C with a larger change trend of 0.16°C/decade.

The application of annual maximum LST data for thermal anomalies detecting during the period 2003–2019 was conducted. The spatial distribution of SAI > 2.5 has used to monitor thermal anomalies, including drought, heat wave, and ice melting. Some thermal anomaly events have been monitored using annual maximum LST data.

References

[1] M. L. Jin and R. E. Dickinson, "Land surface skin temperature climatology: Benefitting from the strengths of satellite observations," *Environ. Res. Lett.*, vol. 5, no. 4, Oct.–Dec. 2010, Art. no. 044004.

[2] C. J. Tomlinson, L. Chapman, J. E. Thornes, and C. Baker, "Remote sensing land surface temperature for meteorology and climatology: A review," *Meteorol. Appl.*, vol. 18, no. 3, pp. 296–306, Sep. 2011.

[3] Z. Wan, P. Wang, and X. Li, "Using MODIS land surface temperature and normalized difference vegetation index products for monitoring drought in the southern great plains, USA," *Int. J. Remote Sens.*, vol. 25, no. 1, pp. 61–72, Jan. 2004.

[4] L. F. Zhang, W. Z. Jiao, H. M. Zhang, C. P. Huang, and Q. X. Tong, "Studying drought phenomena in the continental United States in 2011 and 2012 using various drought indices," *Remote Sens. Environ.*, vol. 190, pp. 96–106, Mar. 2017.

[5] J. Peng *et al.*, "Spatial-temporal change of land surface temperature across 285 cities in China: An urban-rural contrast perspective," *Sci. Total Environ.*, vol. 635, pp. 487–497, Sep. 2018.

[6] D. C. Zhou *et al.*, "Satellite remote sensing of surface urban heat islands: Progress, challenges, and perspectives," *Remote Sens.-Basel*, vol. 11, no. 1, pp. 48, Jan. 2019.

[7] Q. W. Zhuang, S. X. Wu, Y. Y. Yan, Y. X. Niu, F. Yang, and C. H. Xie, "Monitoring land surface thermal environments under the background of landscape patterns in arid regions: A case study in aksu river basin," *Sci. Total Environ.*, vol. 710, Mar. 2020, Art. no. 136336.

[8] L. M. Zhou, Y. H. Tian, S. B. Roy, C. Thorncroft, L. F. Bosart, and Y. L. Hu, "Impacts of wind farms on land surface temperature," *Nature Climate Change*, vol. 2, no. 7, pp. 539–543, Jul. 2012.

[9] S. S. Peng *et al.*, "Afforestation in China cools local land surface temperature," *Proc. Nat. Acad. Sci. USA*, vol. 111, no. 8, pp. 2915–2919, Feb. 2014.

[10] Y. Li, M. S. Zhao, S. Motesharrei, Q. Z. Mu, E. Kalnay, and S. C. Li, "Local cooling and warming effects of forests based on satellite observations," *Nature Commun.*, vol. 6, pp. 1–8, Mar. 2015.

[11] R. Hollmann *et al.*, "The ESA climate change initiative satellite data records for essential climate variables," *Bull. Amer. Meteorol. Soc.*, vol. 94, no. 10, pp. 1541–1552, Oct. 2013.

[12] S. Bojinski, M. Verstraete, T. C. Peterson, C. Richter, A. Simmons, and M. Zemp, "The concept of essential climate variables in support of climate research, applications, and policy," *Bull. Amer. Meteorol. Soc.*, vol. 95, no. 9, pp. 1431–1443, Sep. 2014.

[13] Z. L. Li *et al.*, "Satellite-derived land surface temperature: Current status and perspectives," *Remote Sens. Environ.*, vol. 131, pp. 14–37, Apr. 2013.

[14] S. B. Duan *et al.*, "Influence of adjacency effect on high-spatial-resolution thermal infrared imagery: Implication for radiative transfer simulation and land surface temperature retrieval," *Remote Sens. Environ.*, vol. 245, Aug. 2020, Art. no 111852.

[15] P. Sismanidis, B. Bechtel, I. Keramitsoglou, and C. T. Kiranoudis, "Mapping the spatiotemporal dynamics of europe's land surface temperatures," *IEEE Geosci. Remote Sens. Lett.*, vol. 15, no. 2, pp. 202–206, Feb. 2018.

[16] W. Zhao, J. L. He, G. F. Yin, F. P. Wen, and H. Wu, "Spatiotemporal variability in land surface temperature over the mountainous region affected by the 2008 wenchuan earthquake from 2000 to 2017," *J. Geophys. Res.-Atmos.*, vol. 124, no. 4, pp. 1975–1991, Feb. 2019.

[17] S. Prakash and H. Norouzi, "Land surface temperature variability across India: A remote sensing satellite perspective," *Theor. Appl. Climatol.*, vol. 139, no. 1-2, pp. 773–784, Jan. 2020.

[18] Y. R. Yu *et al.*, "Interannual spatiotemporal variations of land surface temperature in China from 2003 to 2018," *IEEE J. Sel. Topics Appl. Earth Observ. Remote Sens.*, vol. 14, pp. 1783–1795, 2021.

[19] S. B. Duan, Z. L. Li, and P. Leng, "A framework for the retrieval of all-weather land surface temperature at a high spatial resolution from polar-orbiting thermal infrared and passive microwave data," *Remote Sens. Environ.*, vol. 195, pp. 107–117, Jun. 2017.

[20] M. Azarderakhsh, S. Prakash, Y. X. Zhao, and A. AghaKouchak, "Satellite-based analysis of extreme land surface temperatures and diurnal variability across the hottest place on earth," *IEEE Geosci. Remote Sens. Lett.*, vol. 17, no. 12, pp. 2025–2029, Dec. 2020.
[21] D. J. Mildrexler, M. Zhao, W. B. Cohen, S. W. Running, X. P. Song, and M. O. Jones, "Thermal anomalies detect critical global land surface changes," *J. Appl. Meteorol. Climate*, vol. 57, no. 2, pp. 391–411, Feb. 2018.
[22] D. J. Mildrexler, M. S. Zhao, F. A. Heinsch, and S. W. Running, "A new satellite-based methodology for continental-scale disturbance detection," *Ecol. Appl.*, vol. 17, no. 1, pp. 235–250, Jan. 2007.
[23] Z. Wan and J. Dozier, "A generalized split-window algorithm for retrieving land-surface temperature from space," *IEEE Trans. Geosci. Remote*, vol. 34, no. 4, pp. 892–905, Jul. 1996.
[24] A. D., W. J. Zhao, X. Y. Qua, R. Jing, and K. Xiong, "Spatio-temporal variation of vegetation coverage and its response to climate change in north China plain in the last 33 years," *Int. J. Appl. Earth Obstet.*, vol. 53, pp. 103–117, Dec. 2016.
[25] X. W. Duan, Z. J. Gu, Y. G. Li, and H. J. Xu, "The spatiotemporal patterns of rainfall erosivity in yunnan province, southwest China: An analysis of empirical orthogonal functions," *Glob. Planet Change*, vol. 144, pp. 82–93, Sep. 2016.
[26] X. F. Ma, W. Yan, C. Y. Zhao, and Z. W. Kundzewicz, "Snow-cover area and runoff variation under climate change in the west kunlun mountains," *Water*, vol. 11, no. 11, Nov. 2019, Art. no. 2246.
[27] R. H. Grumm and R. Hart, "Standardized anomalies applied to significant cold season weather events: Preliminary findings," *Weather Forecast*, vol. 16, no. 6, pp. 736–754, 2001.
[28] J. A. Sobrino, S. Garcia-Monteiro, and Y. Julien, "Surface temperature of the planet earth from satellite data over the period 2003-2019," *Remote Sens.-Basel*, vol. 12, no. 12, Jun. 2020, Art. no. 2036.
[29] J. A. Sobrino and Y. Julien, "Trend analysis of global MODIS-terra vegetation indices and land surface temperature between 2000 and 2011," *IEEE J. Sel. Topics Appl. Earth Observ. Remote Sens.*, vol. 6, no. 5, pp. 2139–2145, Oct. 2013.
[30] T. R. Karl *et al.*, "U.S. temperature and drought: Recent anomalies and trends," *Eos, Trans. Amer. Geophys. Union*, vol. 93, no. 47, pp. 473–474, 2012.
[31] J. C. Jimenez-Munoz *et al.*, "Record-breaking warming and extreme drought in the amazon rainforest during the course of el nino 2015-2016," *Sci. Rep.*, vol. 6, pp. 1–7, Sep. 2016.
[32] P. A. Stott, D. A. Stone, and M. R. Allen, "Human contribution to the european heatwave of 2003," *Nature*, vol. 432, no. 7017, pp. 610–614, Dec. 2004.
[33] D. Barriopedro, E. M. Fischer, J. Luterbacher, R. Trigo, and R. Garcia-Herrera, "The hot summer of 2010: Redrawing the temperature record map of europe," *Science*, vol. 332, no. 6026, pp. 220–224, Apr. 2011.
[34] A. Shepherd *et al.*, "A reconciled estimate of ice-sheet mass balance," *Science*, vol. 338, no. 6111, pp. 1183–1189, Nov. 2012.
[35] S. V. Nghiem *et al.*, "The extreme melt across the Greenland ice sheet in 2012," *Geophys. Res. Lett.*, vol. 39, no. 20, Oct. 2012, Art. no. L20502.
[36] M. Tedesco *et al.*, "Evidence and analysis of 2012 Greenland records from spaceborne observations, a regional climate model and reanalysis data," *Cryosphere*, vol. 7, no. 2, pp. 615–630, 2013.

Si-Bo Duan (Senior Member, IEEE) received the Ph.D. degree in cartography and geographical information system from the Institute of Geographic Sciences and Natural Resources Research, Chinese Academy of Sciences, Beijing, China, in 2014.

He is currently a Professor with the Key Laboratory of Agricultural Remote Sensing, Ministry of Agriculture and Rural Affairs/Institute of Agricultural Resources and Regional Planning, Chinese Academy of Agricultural Sciences, Beijing, China. His research interest includes the retrieval and validation of land surface temperature.

Cheng Huang received the Ph.D. degree in cartography and geographical information system from the University of Chinese Academy of Sciences, Beijing, China, in 2020.

He is currently a Post-doctoral with the Institute of Agricultural Resources and Regional Planning, Chinese Academy of Agricultural Sciences, Beijing, China. His main research concentration is on retrieval and validation of land surface temperature from passive microwave data, and conversion between TIR and microwave derived land surface temperatures.

Xiangyang Liu received the B.S. degree in land resource management from Hebei Agricultural University, Baoding, China, in 2013, the M.S. degree in cartography and geographic information system from the Yantai Institute of Coastal Zone Research, Chinese Academy of Sciences, Yantai, China, in 2016, and the Ph.D. degree in cartography and geographical information system from the Institute of Geographic Sciences and Natural Resources Research, Chinese Academy of Sciences, Beijing, China, in 2020.

He is currently a Postdoc with the Key Laboratory of Agricultural Remote Sensing, Ministry of Agriculture and Rural Affairs/Institute of Agricultural Resources and Regional Planning, Chinese Academy of Agricultural Sciences, Beijing, China.

His research interests include modeling of thermal radiation directionality and analyses of long-term series land surface temperature.

Meng Liu received the Ph.D. degree in cartography and geographical information system from the Institute of Geographic Sciences and Natural Resources Research, Chinese Academy of Sciences, Beijing, China, in 2019.

She is currently an Assistant Professor with the Institute of Agricultural Resources and Regional Planning, Chinese Academy of Agricultural Sciences, Beijing, China. Her research interests include the retrieval of land surface evapotranspiration and the separation of evaporation and transpiration by remote sensing.

Yingwei Sun received the B.S. degree in remote sensing science and technology from the Shandong University of Science and Technology, Qingdao, China, in 2013, the M.S. degree in geological engineering from the China University of Geosciences, Wuhan, China, in 2017, and the Ph.D. degree in cartography and geographical information system from Aerospace Information Research Institute, Chinese Academy of Sciences, Beijing, China, in 2020.

His research interests include the geographical spatial-multi-temporal data mining and LST anomaly analysis.

Caixia Gao received the B.S. degree in electronic and information engineering from the Xi'an University of Posts and Telecommunications, Xi'an, China, in 2006, the M.S. degree in computer science from the Academy of Opto-Electronics, Chinese Academy of Sciences, Beijing, China, in 2009, and the Ph.D. degree in cartography and geography information system from the University of Chinese Academy of Sciences, Beijing, China, in 2012.

She is currently a Professor with Aerospace Information Research Institute, Chinese Academy of Sciences. Her research interests include in-orbit calibration and validation of optical sensors, and the retrieval of surface temperature and emissivity.